PAPER • OPEN ACCESS

Underwater gas self-transportation along femtosecond laser-written open superhydrophobic surface microchannels (<100 μ m) for bubble/gas manipulation

To cite this article: Jiale Yong et al 2022 Int. J. Extrem. Manuf. 4 015002

View the article online for updates and enhancements.

You may also like

- <u>Triboelectric 'electrostatic tweezers' for</u> manipulating droplets on lubricated slippery surfaces prepared by femtosecond laser processing Jiale Yong, Xinlei Li, Youdi Hu et al.
- TIME-VARYING DYNAMICAL STAR FORMATION RATE Eve J. Lee, Philip Chang and Norman Murray
- FEATHERING INSTABILITY OF SPIRAL ARMS. II. PARAMETER STUDY Wing-Kit Lee

Int. J. Extrem. Manuf. 4 (2022) 015002 (15pp)

https://doi.org/10.1088/2631-7990/ac466f

Underwater gas self-transportation along femtosecond laser-written open superhydrophobic surface microchannels (<100 μ m) for bubble/gas manipulation

Jiale Yong¹, Qing Yang², Jinglan Huo¹, Xun Hou¹ and Feng Chen^{1,*}

E-mail: chenfeng@mail.xjtu.edu.cn

Received 27 September 2021, revised 2 November 2021 Accepted for publication 26 December 2021 Published 14 January 2022



Abstract

Underwater transportation of bubbles and gases has essential applications in manipulating and using gas, but achieving this function at the microscopic level remains a significant challenge. Here, we report a strategy to self-transport gas in water along a laser-induced open superhydrophobic microchannel with a width less than 100 μ m. The femtosecond laser can directly write superhydrophobic and underwater superaerophilic microgrooves on the polytetrafluoroethylene (PTFE) surfaces. In water, the single laser-induced microgroove and water medium generate a hollow microchannel. When the microchannel connects two superhydrophobic regions in water, the gas spontaneously travels from the small region to the large area along this hollow microchannel. Gas self-transportation can be extended to laser-drilled microholes through a thin PTFE sheet, which can even achieve anti-buoyancy unidirectional penetration. The gas can overcome the bubble's buoyance and spontaneously travel downward. The Laplace pressure difference drives the processes of spontaneous gas transportation and unidirectional bubble passage. We believe the property of gas self-transportation in the femtosecond laser-structured open superhydrophobic and underwater superaerophilic microgrooves/microholes has significant potential applications related to manipulating underwater gas.

Original content from this work may be used under the terms of the Creative Commons Attribution 3.0 licence. Any further distribution of this work must maintain attribution to the author(s) and the title of the work, journal citation and DOI.

¹ State Key Laboratory for Manufacturing System Engineering and Shaanxi Key Laboratory of Photonics Technology for Information, School of Electronic Science and Engineering, Xi'an Jiaotong University, Xi'an 710049, People's Republic of China

² School of Mechanical Engineering, Xi'an Jiaotong University, Xi'an 710049, People's Republic of China

Author to whom any correspondence should be addressed.

Supplementary material for this article is available online

Keywords: femtosecond laser, gas transportation, superhydrophobicity, underwater superaerophilicity, water/gas separation

(Some figures may appear in colour only in the online journal)

1. Introduction

The manipulation and use of gas in water have broad applications in energy utilization, chemical manufacturing, environmental protection, agricultural breeding, microfluidic chips, and health care [1-10]. Recently, it has been reported that unique gradient geometries can drive underwater bubbles to move spontaneously and directionally over some distance. For example, Ma et al prepared superaerophilic geometry-gradient polyethylene surfaces that engendered high driving force on the gas bubbles and directionally and continuously transported gas bubbles on open surfaces without energy input [11]. Yu et al fabricated superhydrophobic copper cones by integrating low-surface-tension chemical coatings with conical morphology, which spontaneously transported gas bubbles from their tips to the base in water [12]. The gas self-transportation effect has been successfully applied to manipulate large bubbles. However, the gradient geometry is often macroscopic and cannot transport gas at the microscopic level because the microscale gradient structures do not provide enough driving force. Gas self-transportation at the microscopic level along an underwater microchannel remains a challenge, which has significant potential applications in microfluidics, lab chips, microanalyzers, microdetectors, etc.

Femtosecond (10^{-15} s) lasers have two features, ultrashort pulse width and extremely high peak intensity [13–16], which have become an essential tool for modern extreme and ultra-precision manufacturing. Femtosecond laser processing has the characteristics of high spatial resolution, small heataffected zone, and non-contact manufacturing [17–19]. In particular, the femtosecond laser can ablate almost any material, resulting in microstructures on the material's surface. Because the surface microstructure has a significant effect on the wettability of solid substrates, the femtosecond laser processing shows a powerful ability to design and modify the wettability of materials [13, 14, 20-24]. For example, Baldacchini et al [25] and Zorba et al [26] used femtosecond lasers to create superhydrophobic microstructures on silicon surfaces under SF₆ gas. Yong et al obtained superhydrophobicity on various polymer substrates by femtosecond laser treatment [27–31].

In this paper, we induce gas self-transportation along an open superhydrophobic microchannels with a width <100 μ m. The femtosecond laser-induced hierarchical micro/nanostructures promotes superhydrophobicity in air and excellent underwater superaerophilicity on the polytetrafluoroethylene (PTFE) surface. Immersing the PTFE surface with superhydrophobic microgrooves in water generates hollow microchannels between the PTFE substrate and the water medium. Underwater gas can flow through this channel. When a microchannel connects two underwater bubbles,

the gas spontaneously transports from the small bubble to the large bubble along this hollow microchannel. Gas selftransportation can be extended to more functions related to manipulating bubbles underwater, such as unidirectional gas passage and water/gas separation.

2. Results and discussion

2.1. Femtosecond laser writing superhydrophobic microchannels

Hierarchical microstructures should be built on the substrate with low surface energy to obtain underwater superaerophilicity [32-35]. PTFE sheet was adopted in this experiment because of its remarkably intrinsic hydrophobicity. A water droplet on an untreated PTFE substrate has a water contact angle (WCA) of $111.0 \pm 0.5^{\circ}$ in the air (figure S1(a), supporting information available online at stacks.iop.org/IJEM/4/015002/mmedia). The bubble contact angle (BCA) of a small bubble on this surface is $113.0 \pm 1.8^{\circ}$ in water (figure S1(b), supporting information). The original PTFE surface shows high adhesion to water droplets and gas bubbles (underwater) as they firmly sticks to the PTFE surface (figures S1(c) and (d), supporting information). Microscale and nanoscale structures can be easily produced on a given material surface by femtosecond laser processing [13, 16, 18, 36–40]. The femtosecond laser was used to induce hierarchical microstructures on the PTFE substrate. Figure 1(a) shows the femtosecond laser processing system. The PTFE sheet was mounted on a program-controlled translation stage. The laser pulses were focused onto the PTFE surface by a lens. During femtosecond laser treatment, the lineby-line scanning manner (figure 1(b)) was used to process the PTFE surface [29, 41].

The interaction between the femtosecond laser and the PTFE surface is a nonlinear light-absorption process, as shown in figure 1(c) [13–15, 17, 18]. The extremely high intensity enables the femtosecond laser pulses to directly trigger the avalanche ionization via a multiphoton ionization mechanism. Carriers can be thermally excited from traps or defects. With the carriers acting as the seed electrons in the conduction band, the avalanche ionization occurs and results in that the conduction band electrons are having an exponential increase. The density of free carriers in the plasma rapidly increases in multiphoton ionization and avalanche ionization. The laser energy is primordially absorbed by free electrons, resulting in the remarkable increase of the kinetic energy of the free electrons. Meanwhile, part of the absorbed energy is instantly transferred to the lattice. And finally, hightemperature and high-pressure plasmas form above the PTFE

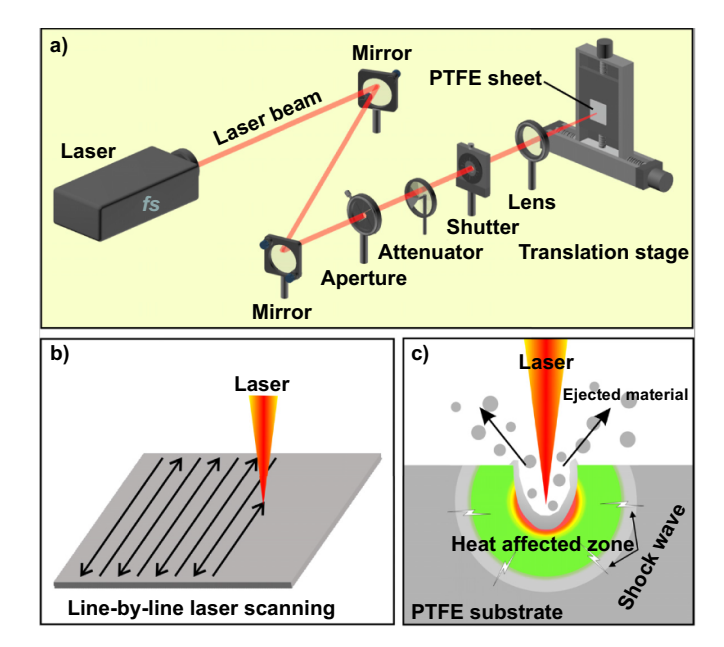


Figure 1. Schematic of preparing superhydrophobic and underwater superaerophilic surface microstructures on the PTFE surface by laser processing. (a) Equipment diagram for laser microfabrication. (b) Line-by-line laser scanning manner. (c) Schematic interaction between the femtosecond laser pulses and PTFE substrate.

substrate. The ions and the electrons reach a thermal equilibration state over a timescale of picoseconds. The accumulation of kinetic energy within the focal volume of the PTFE substrate is limited. The ions will instantaneously vaporize from the melt phase. As the plasma with high pressure and high temperature instantaneously expands and bursts out of the ablation spot, the ionized materials are removed from the substrate surface [13–15, 17, 18]. The ejection of the ablated material results in permanent damage of the substrate and generates rough surface microstructures on the substrate. When part of the ejected molten particles falls back, fine nano-protrusions further self-assembly cover on the ablated surface after the solidification of the ejected particles. As a result, micro/nanostructures form on the sample surface after femtosecond laser processing [13–15, 17, 18].

Figures 2 and S2 (supporting information) show the scanning electronic microscopy (SEM) images of the PTFE surfaces that are ablated by a femtosecond laser with the laserscanning interval (Λ) ranging from 25 μ m to 150 μ m. Each laser scanning line can produce a groove structure on the sample surface because of the laser-induced material removal. The width of the laser-induced groove is \sim 91.5 μ m, and the depth is \sim 53.0 μ m (figures 2(a) and S2(a)) under the laser fluence of \sim 24 J cm⁻² and scanning speed of 5 mm s⁻¹. In addition, the inner wall of the microgroove is covered with fine microstructure and nanostructure. When the Λ is 150 μ m, the microgrooves are entirely separated (figures 2(a) and S2(a)). Apparent flat domains exist between the laser-induced microgrooves, which are not ablated by femtosecond laser. As the Λ decreases, the microgrooves get closer and closer (figures 2(a)–(c) and S2(a)–(c)). In the case of $\Lambda = 100 \ \mu \text{m}$, a small unablated area can still be observed (figures 2(c) and S2(c)). As Λ decreases further, the microgrooves overlap, and no unablated area is left (figures 2(d)–(f) and S2(d)–(f)). Laser-induced microstructures cover the whole sample surface. The surface still has the apparent microgroove structure at $\Lambda=75~\mu m$ (figures 2(d) and S2(d)). As the Λ decreases to 25 μm , the adjacent microgrooves have a substantial overlap so that the basic groove structure gradually disappears (figures 2(f) and S2(f)).

Figures 3(a)-(c) shows the magnified SEM images of the laser-induced microstructures on the PTFE substrate $(\Lambda = 75 \mu m)$. In addition to the microgrooves (figure 3(a)), abundant fine protrusions and pores are randomly distributed throughout the entire sample surface (figure 3(b)). The shapes of the protrusions are irregular, and the size of the protrusions ranges from 1.5 μ m to 6.5 μ m. The surface of the protrusions is also coated with particles-like nanostructure with the size of a few hundred nanometers (figure 3(c)). Such micro/nanoscale hierarchical structures are directly written on the PTFE surface by a one-step femtosecond laser process. The laser-ablated surface can support water droplets in a spherical shape without any chemical treatment (figure 3(d)). The droplets have a WCA of 154.0 \pm 0.7° (figure 3(e)). When the PTFE surface is tilted to $4.0 \pm 0.5^{\circ}$, the water droplet can roll away rapidly; that is, the water sliding angle (WSA) is only $4.0 \pm 0.5^{\circ}$ (figure 3(g) and movie S1 in the supporting information). The acceleration of the droplet is about 65 mm s^{-2} at the beginning of the rolling process. The rolling velocity of the droplet can reach up to 6.5 cm s⁻¹ within 1 s. If a tiny water droplet freely falls and impacts the surface, the droplet will rebound many times (figure 3(h) and movie S2 in the supporting information). The resultant PTFE surface exhibits superhydrophobicity and low adhesion to water. A mirror-like interface appears on the PTFE surface when the superhydrophobic surface is dipped into water (figure 3(f)). It is caused by the trapped air film between water and the laser-induced superhydrophobic microstructure [42, 43]. In this case, if a bubble touches the PTFE surface, it can quickly spread over the sample surface (figure 3(i) and movie S3 in the supporting information). Because of the whole spread, the BCA of the bubble is expected to be close to 0°. Therefore, the laser treatment also makes the PTFE surface superaerophilic in water.

Figure 4 reveals the underlying reason for the superhydrophobicity and underwater superaerophilicity of the PTFE surface after femtosecond laser processing. The synergistic effect between the laser-induced hierarchical microstructure and the hydrophobic chemical composition inhibits water penetration into the surface microstructure of the PTFE substrate [43–46]. As shown in figure 4(a), the surface microstructures support water, and it is hard to wet the sample surface. Water only contacts with the peak part of the hierarchical microstructure of the structured PTFE surface and is in the Cassie state on the sample surface [45, 46]. Therefore, the laser-induced microstructure gives excellent superhydrophobicity to the PTFE because the contact area between the water and the PTFE surface is significantly reduced. An air cushion exists between the water and the PTFE substrate. When the sample is immersed in water, the surface microstructures are still not wetted by the water environment. An air

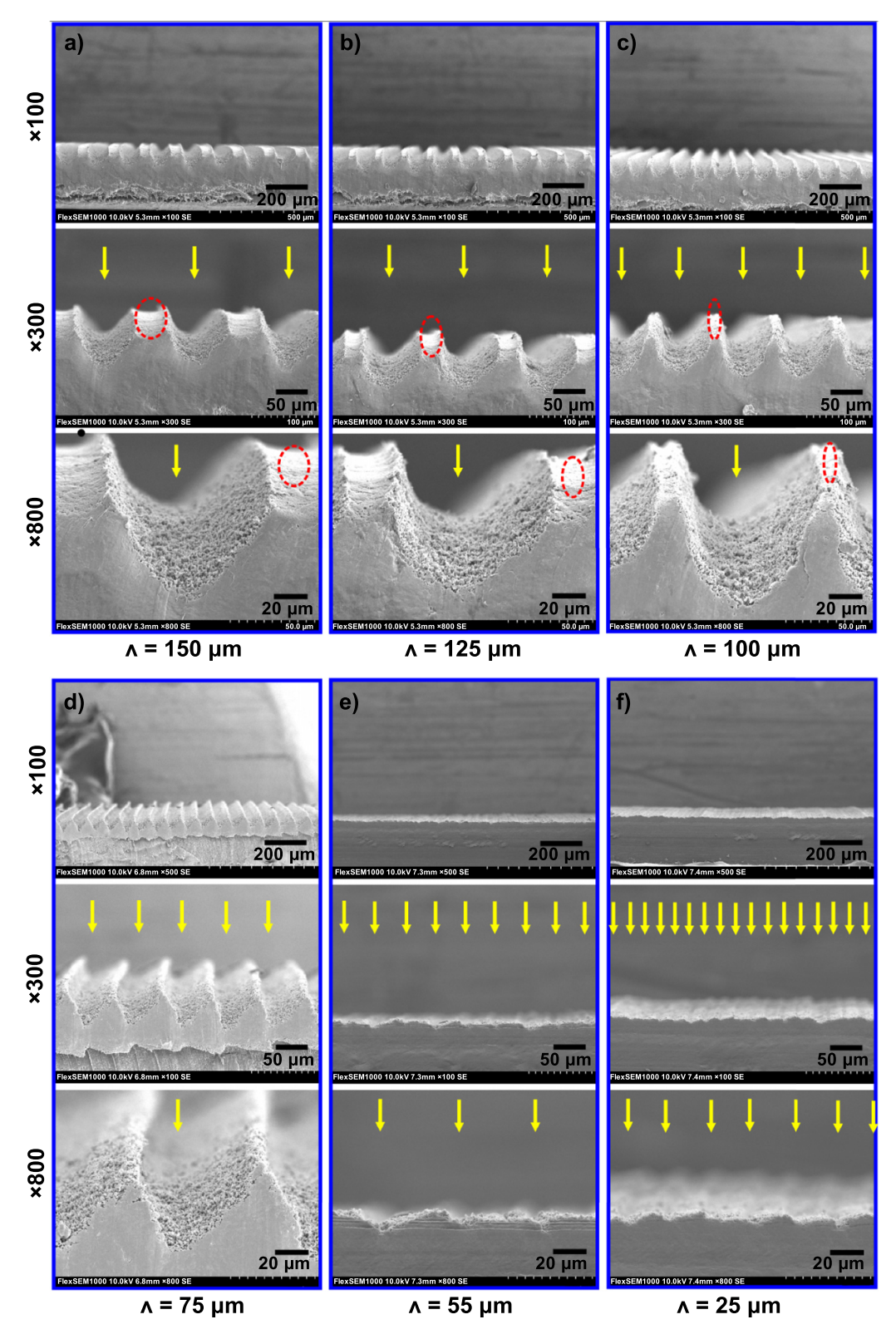


Figure 2. Cross-sectional SEM images of the femtosecond laser-processed PTFE surface at the scanning interval (Λ) of (a) 150 μ m, (b) 125 μ m, (c) 100 μ m, (d) 75 μ m, (e) 50 μ m, and (f) 25 μ m. The yellow arrows indicate the location of the laser scanning lines. The red dotted circles show the flat domains without laser ablation.

film forms between the PTFE and water medium (figure 4(b)). Once a bubble contacts the sample surface, the bubble connects with this trapped air film (figure 4(c)). The bubble's surface tension and high pressure drive the gas in the bubble

to spread along with the trapped air film on the sample surface (figure 4(d)) [43, 44]. Therefore, the femtosecond laser-induced PTFE microstructure appears superaerophilic in water.

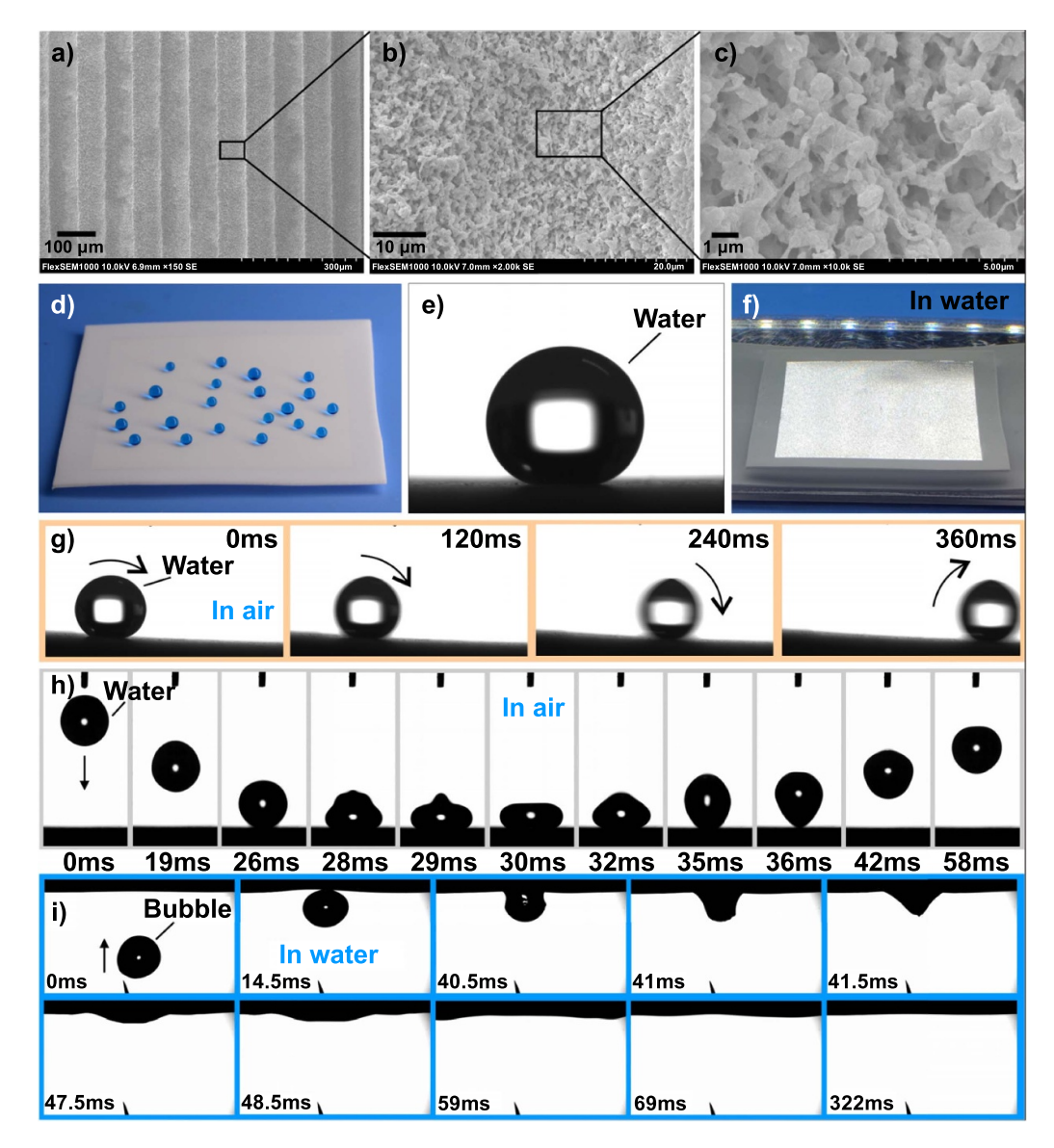


Figure 3. Wettability of the laser-processed PTFE surface ($\Lambda=75~\mu m$). (a)–(c) SEM images of the surface microstructures on the PTFE sheet. (d) Photo of water droplets (blue color) on the PTFE surface. (e) Shape of a water droplet on the resultant PTFE sheet. (f) Photo of the laser-structured PTFE sheet in water. (g) Rolling process of a water droplet on the sample surface. (h) Fall-down water droplet rebounding off the laser-ablated PTFE surface. (i) Process of a bubble spreading over the laser-treated PTFE surface in water.

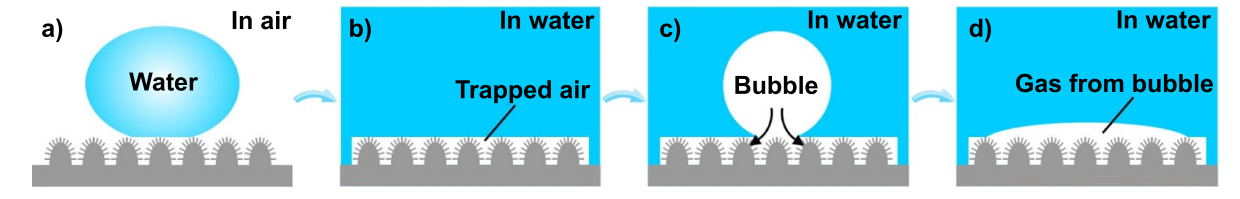


Figure 4. Formation mechanism of the superhydrophobicity and underwater superaerophilicity of the femtosecond laser-structured PTFE surface. (a) Cassie contact state between the surface microstructure of the ablated PTFE and water in the air. (b) Structured PTFE surface in a water medium. (c) Bubble coming in contact with the structured PTFE surface. (d) Gas in the bubble spreading over the sample surface underwater.

Figure S3 (supporting information) shows the influence of the scanning interval (the most crucial machining parameter) on the surface wettability of the laser-processed PTFE substrate. When the $\Lambda < 100~\mu m$, the whole PTFE surface is covered by laser-induced micro/nanostructures. All samples

have excellent superhydrophobicity, with a WCA larger than 150° and a WSA less than 10°, as shown in figures S3(a) and (c). When the Λ increases from 100 μm to 200 μm , the WCA value gradually reduces from 154.5 \pm 0.4° to 141.0 \pm 2.0°. The WCA continuously decreases to 111.0 \pm 0.5° as the

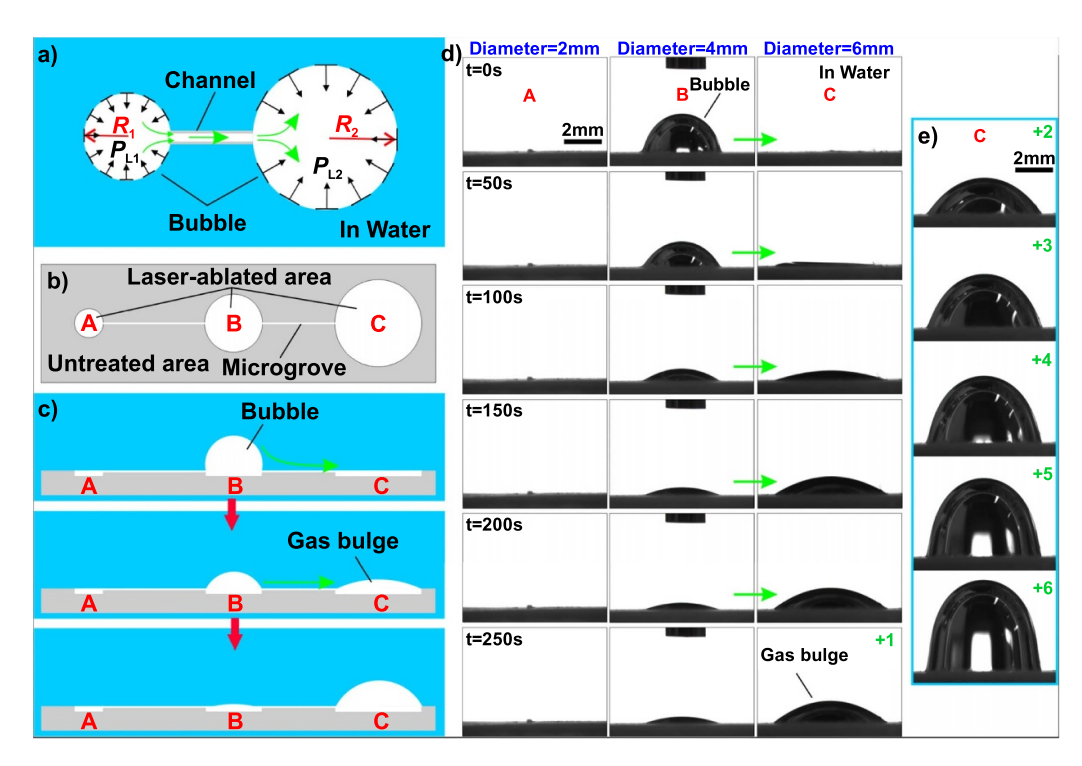


Figure 5. Spontaneous gas transportation along the laser-induced superhydrophobic microgroove in water. (a) Schematic of gas transportation from a small bubble to a big bubble along a contacting channel. (b) Schematic of the femtosecond laser-induced microgroove connecting three superhydrophobic circular regions on the PTFE surface. The diameters of the circular regions are 2 mm (A region), 4 mm (B region), and 6 mm (C region), respectively (from left to right). (c) Schematic of the process of gas transportation from the superhydrophobic region with a smaller area to the region with a larger area. (d) Experimental result of the bubble change after being dispensed onto the B region on the PTFE sample in water. The first column, the second column, and the third column are the images of the A region, B region, and C region, respectively. (e) Volume increase of the gas bulge in the C region with more bubbles being dispensed onto the B region.

 Λ reaches $+\infty$ for an untreated flat PTFE surface. So, the degree of hydrophobicity declines with Λ growth. Meanwhile, the adhesion between the water droplet and PTFE surface continues to increase. The WSA increases from $3.3\pm0.4^{\circ}$ to 90° as the Λ enlarges from 100 μ m to 175 μ m. WSA = 90° is defined as water droplets that firmly attach to the sample surface even when the sample is placed vertically. All the laserstructured PTFE surfaces with $\Lambda \geqslant 200~\mu \mathrm{m}$ show extremely high adhesion to water. Increased adhesion is also an aspect of reduced hydrophobicity. Regarding underwater bubbles on the PTFE surface (figures S3(b) and (c)), the BCA maintains below 10° when the Λ is no more than 125 μ m. In these cases, the laser-treated PTFE surfaces exhibit underwater superaerophilicity. As the Λ increases from 125 μ m to 200 μ m and then to $+\infty$, the BCA value gradually increases from $7.9 \pm 1.1^{\circ}$ to $65.8 \pm 18.8^{\circ}$ and then to $113.0 \pm 1.8^{\circ}$. So, the increase of the Λ also results in a decline of the underwater aerophilicity of the PTFE surface. The fall of the in-air hydrophobicity and underwater aerophilicity is due to the fact that the area fraction of the laser-induced microstructures to the whole sample surface decreases with increasing Λ .

2.2. Underwater gas self-transportation

A single femtosecond laser-induced microgroove has superhydrophobic and underwater superaerophilic micro/

nanostructures on its inner wall. The microgroove cannot be wetted by water so a hollow microchannel forms between PTFE substrate and water as the groove-structured PTFE surface is immersed in water. The width of the laser-induced microgroove determines the width of the hollow microchannel, which is less than $100~\mu m$. Gas can freely flow along the underwater microchannel; that is, this microchannel enables gas transport in water.

Gas transportation will occur between two bubbles in a water medium if a laser-induced channel connects them. As shown in figure 5(a), if the connected bubbles have different sizes, their Laplace pressures differ due to the different radiuses of curvature. According to the Young–Laplace equation, the difference in Laplace pressure, $\Delta P_{\rm L}$, can be described as [47–51]:

$$\Delta P_{\rm L} = P_{\rm L1} - P_{\rm L2} = \gamma \left(\frac{1}{R_1} - \frac{1}{R_2} \right) \tag{1}$$

where P_{L1} and P_{L2} are the differential Laplace pressures. R_1 and R_2 are the radiuses of curvature of the two bubbles, respectively. γ is the surface tension of water. This equation reveals that the Laplace pressure of a smaller bubble is more significant than that of a bigger bubble. Such a Laplace-pressure difference can promote gas transportation from a small bubble to a big bubble. To verify this function, we prepare a single microgroove that connects different regions

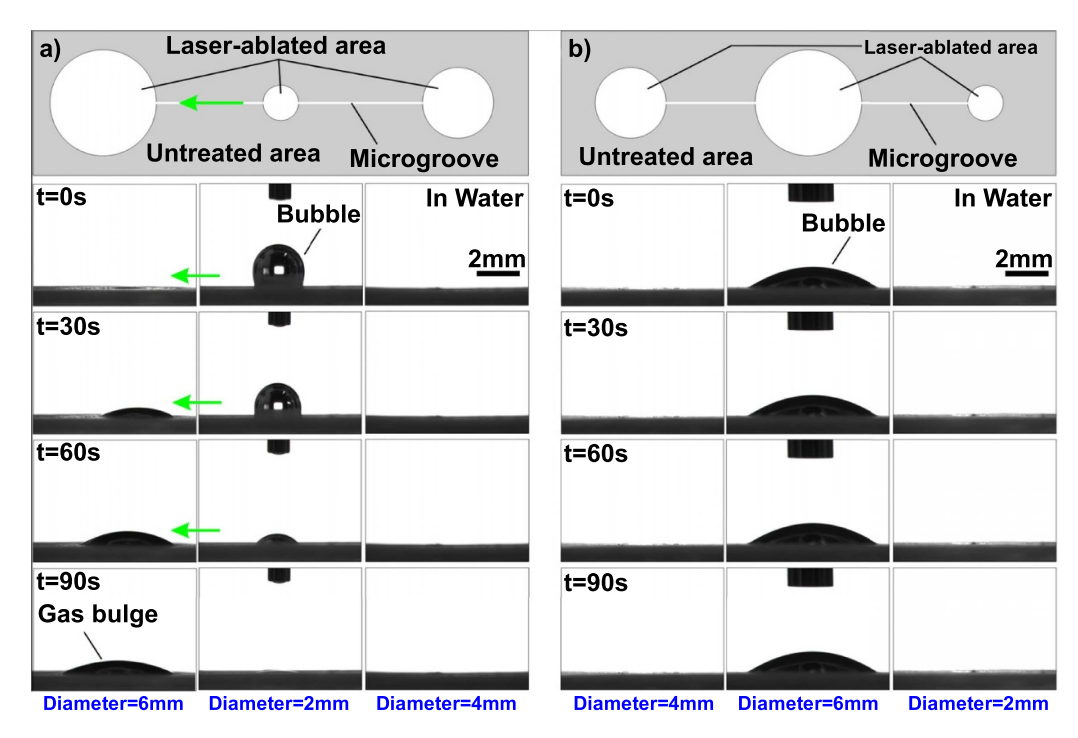


Figure 6. Comparison of the spontaneous gas transportation in the conditions of (a) the superhydrophobic circular regions having the diameters of 6 mm, 2 mm, and 4 mm and (b) the superhydrophobic circular regions having the diameters of 4 mm, 6 mm, and 2 mm from left to right.

on the PTFE substrate. As shown in figure 5(b), three superhydrophobic circular regions are prepared on the surface of a PTFE sheet by laser processing. The circular regions have a diameter of 2 mm (A region), 4 mm (B region), and 6 mm (C region), respectively. The circular regions are entirely covered with laser-induced surface microstructure. Then, a microgroove fabricated by a single femtosecond laser scanning line is integrated to connect these three regions.

Figure 5(d) and movie S4 (supporting information) show the result after dispensing a small bubble (\sim 17 μ 1) onto the B region. It is observed that the bubble becomes smaller and smaller, and the volume of the bubble gradually decreases over time. Meanwhile, a gas film bulges out of the C region. The gas bulge slowly grows bigger, indicating that the gas in the bubble can successfully transfer along the laser-induced microgroove in water. The flow velocity of the gas is measured to be \sim 4.1 μ l min⁻¹. Although this velocity is far smaller than that of the gas transportation on the macroscopic superhydrophobic geometry-gradient surfaces [11, 12], the gas is proven to flow along open microchannels with the width even less than 100 μ m. Dispensing more bubbles onto the B region causes all of the bubbles to disappear from the B region. The volume of the gas bulge in the C region keeps increasing because of the bubble accumulation (figure 5(e)). By contrast, nothing happens in the A region. The results demonstrate that the gas can only transfer from the superhydrophobic region with a smaller area to the region with a larger size, as shown in figure 5(c). This transportation direction is in agreement with the implications of equation (1) and figure 5(a). Furthermore, the process of gas transportation happens spontaneously without any external forces. The Laplace pressure difference between the gas phases in different regions drives the gas self-transportation along the superhydrophobic microgroove in water. From a thermodynamics perspective, the spontaneous transportation of gas from a smaller area to a larger area occurs in the direction of Gibbs free energy reduction until equilibrium [52].

The process of spontaneous gas transportation is also available for other orders of the circular regions. In figure 6(a), the diameters of the superhydrophobic circles are 6 mm, 2 mm, and 4 mm from left to right. A laser-induced microgroove also connects these three circular regions. When a bubble (\sim 5 μ l) is dispensed onto the middle region, the gas in the bubble flows to the left largest circular regions along the microgroove. The surface of the right circular region does not change because its diameter is smaller than that of the left circular region. This result verifies the conclusion mentioned above that gas tends to transport from a small bubble to a large bubble and suggests that the gas will flow to the biggest region if there are multiple large regions. Figure 6(b) presents the condition that the largest circular region is located in the middle. From left to right, the diameters of superhydrophobic circles are 4 mm, 6 mm, and 2 mm, respectively. In this case, when a bubble $(\sim 17 \mu l)$ is dispensed onto the middle region, the gas in the bubble stays above this region over time. No gas bulges appear on both the left and the right circular areas. The gas does not flow from the middle region to the other two regions, because the central region is the largest.

The superhydrophobic microgrooves can provide microchannels for transporting gas underwater. With the Laplace pressure difference between the ends of the microchannel, the gas is driven to spontaneously flow

along the laser-induced microgrooves. The underwater self-transportation of gas can be achieved even when the width of the open superhydrophobic microgrooves is less than 100 μ m. Compared with the tiny channels inside the material, the preparation of the open superhydrophobic microgrooves is more straightforward and more accessible. Transportation of small amounts of gas underwater is a technology with great potential. Microfluidic technology is already well understood [53–55]. Microfluidic systems use microchannels to manipulate tiny fluids (nanoliter in volume). Microfluidics can perform various micro-processing and micro-operations that are difficult to complete by conventional methods. Therefore, it has critical applications in biomedical, chemistry, fluid physics, microelectronics, etc. Like microfluidic technology, gas self-transportation along the superhydrophobic and underwater superaerophilic microgrooves can potentially be used to implement 'aerofluidics,' which fundamentally aims at manipulating gases and fluids at the microscale and exploiting their interaction to create highly versatile systems. It is believed that aerofluidics will have pioneering applications in microanalysis, biomedical engineering, sensors, and other fields.

2.3. Unidirectional gas passage

In addition to the open superhydrophobic microgrooves on the surface of the PTFE sheet, microholes that go through the sheet may also influence the transportation of gas in water. Figure 7(a) depicts the process of preparing a 'Y'-shaped hole on the as-prepared superhydrophobic and underwater superaerophilic PTFE sheet by femtosecond laser drilling. The preparation process involves three steps: deceleration, stopover, and acceleration. In the deceleration process, the relative translational speed of the laser focus to the PTFE sheet gradually decreases along the movement direction. Lower speed means more laser pulses acting on a unit area, resulting in a higher etching depth by laser ablation [30, 56]. Therefore, the ablation depth increases with the laser moving forward. When the laser focus reaches the specified location and the translational speed of the laser focus decreases to 0 mm s⁻¹, the movement of the laser focus stops and stays here for a while. This is the stopover process. Because of the continuous accumulation of laser pulses at this point, the laser can ablate through the PPFE sheet. Then, the laser point moves forward, and its translational speed gradually increases from 0 mm s⁻¹. The result of the acceleration process is opposite to that of the deceleration process. Higher speed means fewer laser pulses acting on a unit area, resulting in a smaller etching depth by laser ablation. Therefore, the ablation depth decreases as the laser moves forward. As a result, a single 'Y'-shaped hole forms on the PTFE sheet. By repeating the above fabrication process, a series of such holes can be prepared. Figures 7(b)–(d) show the morphology of the top part of the laser-induced holes. The holes have an elongated mouth. The long mouth diameter of the hole edge along the movement direction of the laser focus reaches up to \sim 150 μ m. The short mouth diameter of the holes is \sim 40 μ m. Figures 7(e)–(g) shows the bottom part of the as-prepared microholes. The bottom of the microholes is a cylindrical channel with a diameter of $15-20 \mu m$. The diameter of the direct channel of the microhole is only about $17 \mu m$ (figure 7(g)). Therefore, the microholes pass through the thin PTFE sheet and present 'Y' shapes which are composed of the infundibular mouth (top part) and the cylindrical channel (bottom part), as shown in figure 7(h).

The 'Y'-shaped microholes are asymmetric relative to the plane of the PTFE sheet. Such an asymmetric microstructure has a significant influence on the dynamic behavior of bubbles in the water. Figure 8(a) shows the result of a bubble coming in contact with the lower side of the porous superwetting PTFE sheet in a water medium. In this case, the big mouth of the microholes points upward. The bubble can penetrate the PTFE sheet from the lower side to the upper side after contacting with the sheet. A small gas bulge forms on the upper side of the sheet. Releasing more bubbles causes them to pass through the sheet one by one. The bulge volume gradually increases as the gas continuously accumulates, as shown in figure 8(b). Once the volume of the gas bulge is large enough, the high buoyance will lift the gas bulge off the PTFE surface and rise again (figure 8(c)). Therefore, the bubbles successfully pass through the porous sheet; that is, gas spontaneously transports through the porous sheet (movie S5 in the supporting information).

Figures 7(i)-(k) depict the underlying mechanism of the passage of the air bubbles based on kinetic analysis. When the porous sheet is immersed in water, an air film is trapped between the upper superhydrophobic surface microstructures and the surrounding water. Regarding the lower surface of the sheet, water can completely contact the flat unablated area apart from the structure of the holes. Water is unable to enter into the microholes because of the superhydrophobicity of the laser-induced microstructures. Once a spherical air bubble makes contact with the lower surface of the porous sheet, the open microholes act as air channels that connect the spherical bubble and the upper air film (figure 7(i)). At present, there is a significant difference between the radiuses of the air bubble and the trapped air film. The difference in the surface tensions of the spherical bubble and the upper trapped air film gives rise to a difference of Laplace pressure between the lower-side bubble and the upper-side air film. The difference of the differential Laplace pressure can be expressed as [47–51]:

$$\Delta P_{\rm L} = \gamma \left(\frac{1}{R_{\rm down}} - \frac{1}{R_{\rm up}} \right) \tag{2}$$

where $R_{\rm down}$ and $R_{\rm up}$ are the radius of curvature of the gas part on porous sheet's lower and upper sides, respectively. In this case, the lower gas is the bubble, and the upper gas is the trapped air film. Because the air film on the upper side of the porous sheet is broad and smooth, $R_{\rm up}$ is approaching infinity. The $R_{\rm down}$ is much less than that of $R_{\rm up}$, so that the Laplace pressure of the lower bubble is significantly higher than that of the upper air film. The differential Laplace pressure reaches up to several dozens or even hundreds Pa for a small bubble. Because of the Laplace pressure difference between the lower bubble and the upper air film, the gas in the bubble can spontaneously travel along the microholes and

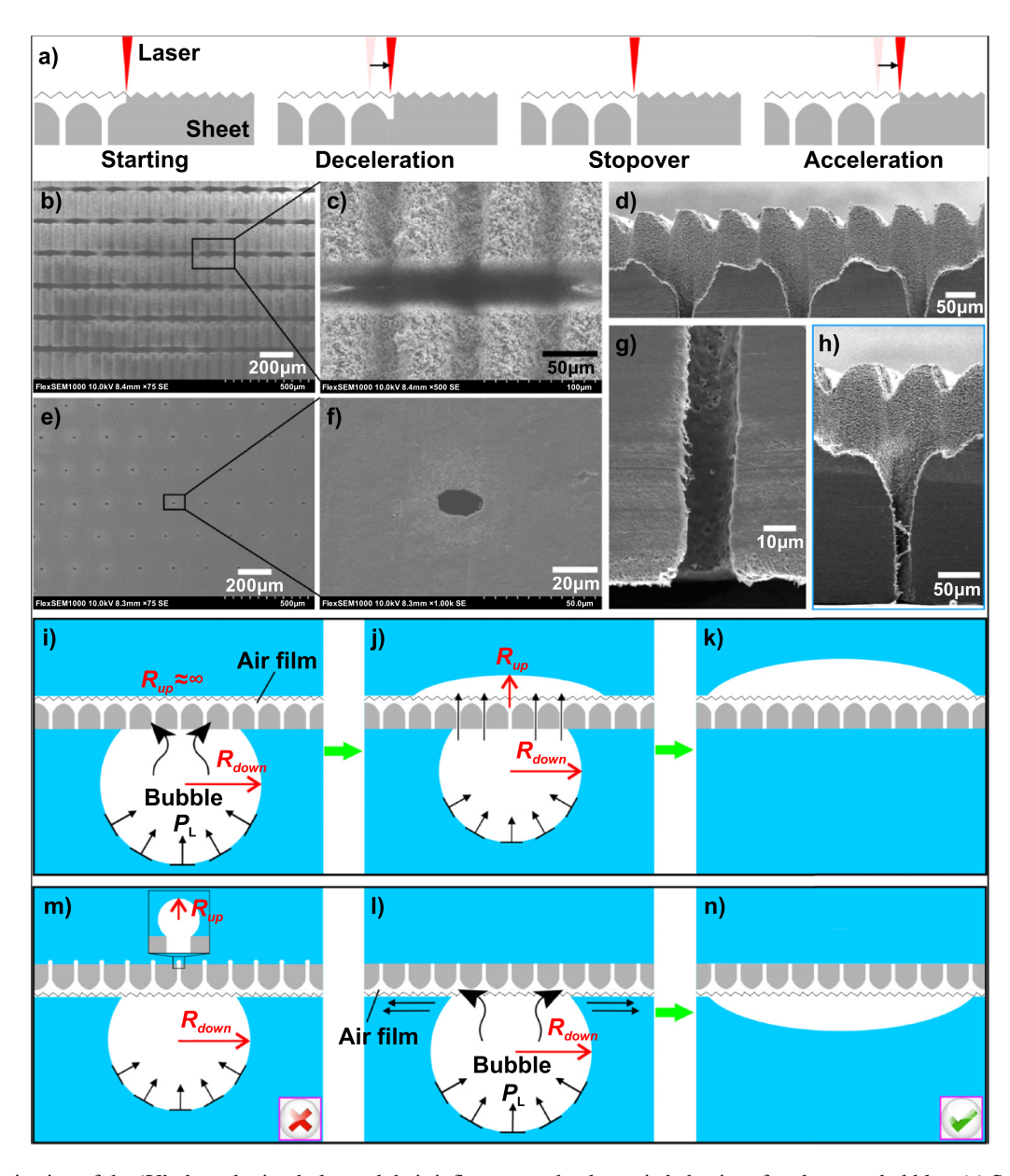


Figure 7. Fabrication of the 'Y'-shaped microholes and their influence on the dynamic behavior of underwater bubbles. (a) Schematic diagram of fabricating a microhole on the superwetting PTFE sheet by femtosecond laser processing. (b), (c) Top-viewed and (d) cross-sectional SEM images of the top part of the laser-induced holes. (e), (f) Top-viewed and (g) cross-sectional SEM images of the bottom part of the laser-induced holes. (h) Cross-sectional SEM image of the whole morphology of the 'Y'-shaped microhole composed of the infundibular mouth (top part) and the cylindrical channel (bottom part). (i)–(k) Underlying passage mechanism of bubble through the porous sheet: (i) a bubble touching the lower side of the sheet, (j) the gas penetrating the sheet along the microholes and entering into the upper air film, and (k) the bubble completely arriving at the upper side of the sheet. (l)–(n) Underlying mechanism of bubbles interception by the porous PTFE sheet: (l) a bubble touching the lower side of the sheet, (m) a hypothetical case that the released bubble below the sheet has a tendency to be transported upwards, and (n) bubble spreading out along the lower surface of the sheet. The big mouth of the microholes in (i)–(k) points upward, while that in (l)–(n) points downward.

finally enter into and merge with the upper air film. So, the bubbles pass through the porous sheet from bottom to top, driven by the Laplace pressure difference.

If the porous PTFE sheet is placed upside down, the effect of the porous sheet on the bubbles is different from the above situation. As shown in figure 8(d), the big mouth of the microholes points downward. A bubble immediately spreads over the lower surface rather than penetrating the sheet after touching the lower side of the porous PTFE sheet. The continuous

arrival of new bubbles causes the bubbles to spread over and accumulate below the sheet (figure 8(e)). In this case, the underwater bubbles cannot penetrate the sheet (movie S6 in the supporting information). Water can completely contact the smooth area of the upper surface, making the holes separate from each other (figure 7(1)). Assume that the released bubble below the sheet tends to be transported upwards, an array of small gas balls will first blow out the microholes on the upper side of the sheet, as shown in figure 7(m). The bottom of the

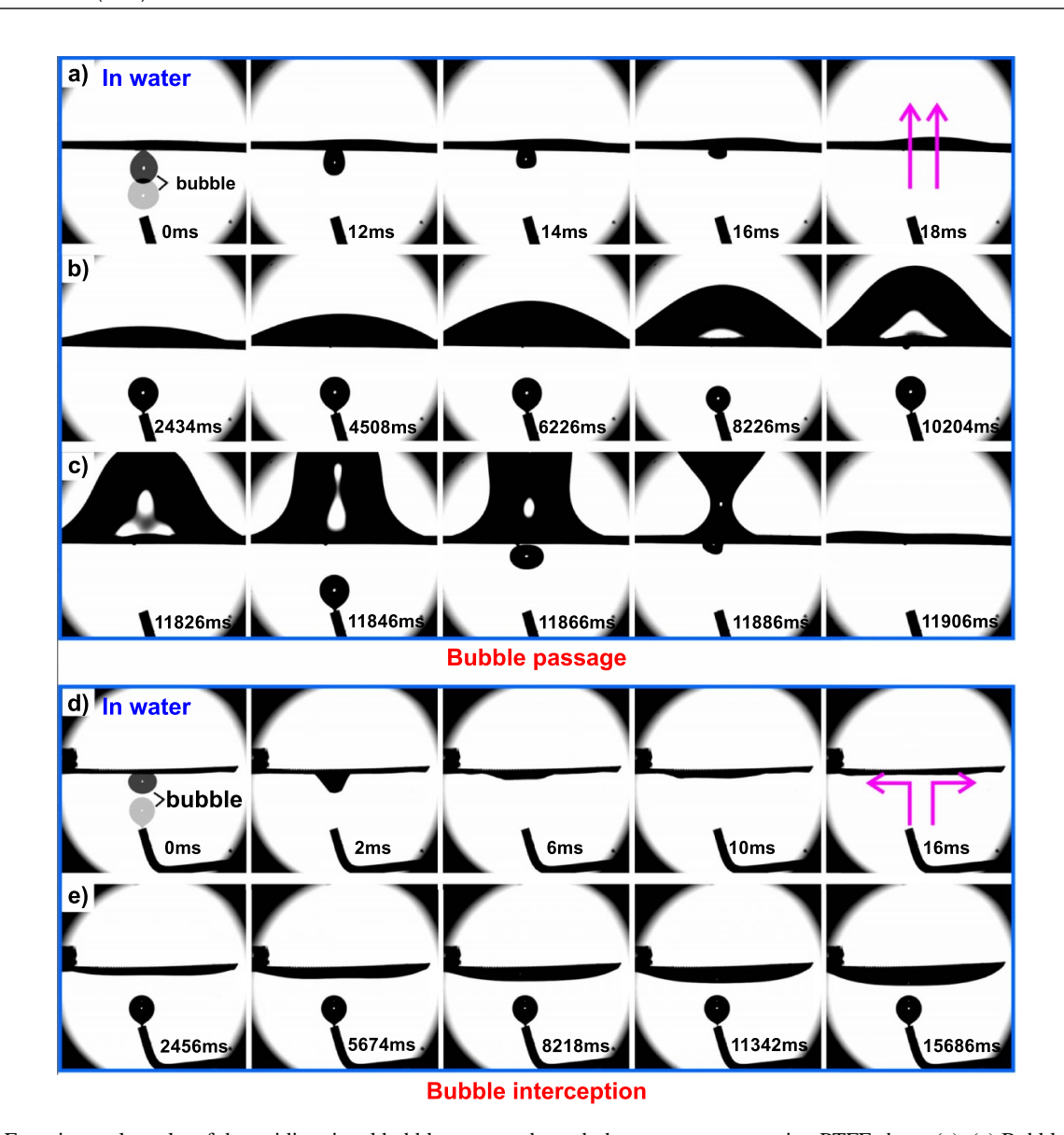


Figure 8. Experimental results of the unidirectional bubble passage through the porous superwetting PTFE sheet. (a)–(c) Bubbles penetrating the porous PTFE sheet from the lower side to the upper side: (a) process of the first bubble passing through the sheet, (b) increasing the number of the released bubbles, and (c) the upper gas bulge detaching from the PTFE sheet. (d), (e) Bubbles stopping below the PTFE sheet: (d) process of the first bubble contacting with the lower side of the sheet and spreading out and (e) more and more bubbles being intercepted below the sheet. The big mouth of the microholes in (a)–(c) points upward, while that in (d), (e) points downward.

microholes is very small, so the radius of the hypothetical upper gas balls is also very small, much smaller than that of the lower air bubble ($R_{\text{down}} > R_{\text{up}}$). At present, the Laplace pressure of the upper gas balls will be larger than that of the lower bubble. The analysis disproves the hypothesis; that is, the passage of the bubbles from the lower side to the upper side of the PTFE sheet is not allowed. To reduce the Laplace pressure of the bubble, the gas of the bubble immediately enters into the air film trapped on the lower side of the PTFE sheet and then spreads horizontally (figure 7(n)) so that the bubbles cannot pass through the sheet from top to bottom. Therefore, the gas bubbles are only allowed to unidirectionally pass through the as-prepared porous PTFE sheet in the water. Such a function is ascribed to the asymmetric morphology of the femtosecond laser-induced 'Y'-shaped microholes and the unique surface superwettability of the PTFE sheet.

The as-prepared porous superwetting PTFE sheet can not only unidirectionally transport gas along the buoyancy direction but can also achieve anti-buoyancy unidirectional penetration. In the water medium, the big mouth of the microholes of the porous sheet points downward. Once the bubbles are moved to contact the upper side of the sheet, they can spontaneously penetrate downward, and a slight gas bulge appears below the sheet (figure 9(a) and movie S7 in the supporting information). In this self-transportation process, the bubble overcomes the constraint of buoyancy. As shown in figure 9(b), there exists a difference in the Laplace pressures of the bubble on the upper PTFE sheet and the trapped air film on the lower sheet. The bubble suffers three forces: downward Laplace force (F_L) , upward buoyancy (F_B) , and upward resistance force (F_R) . According to equation (2), the Laplace pressure difference is significant enough to generate a large $F_{\rm L}$

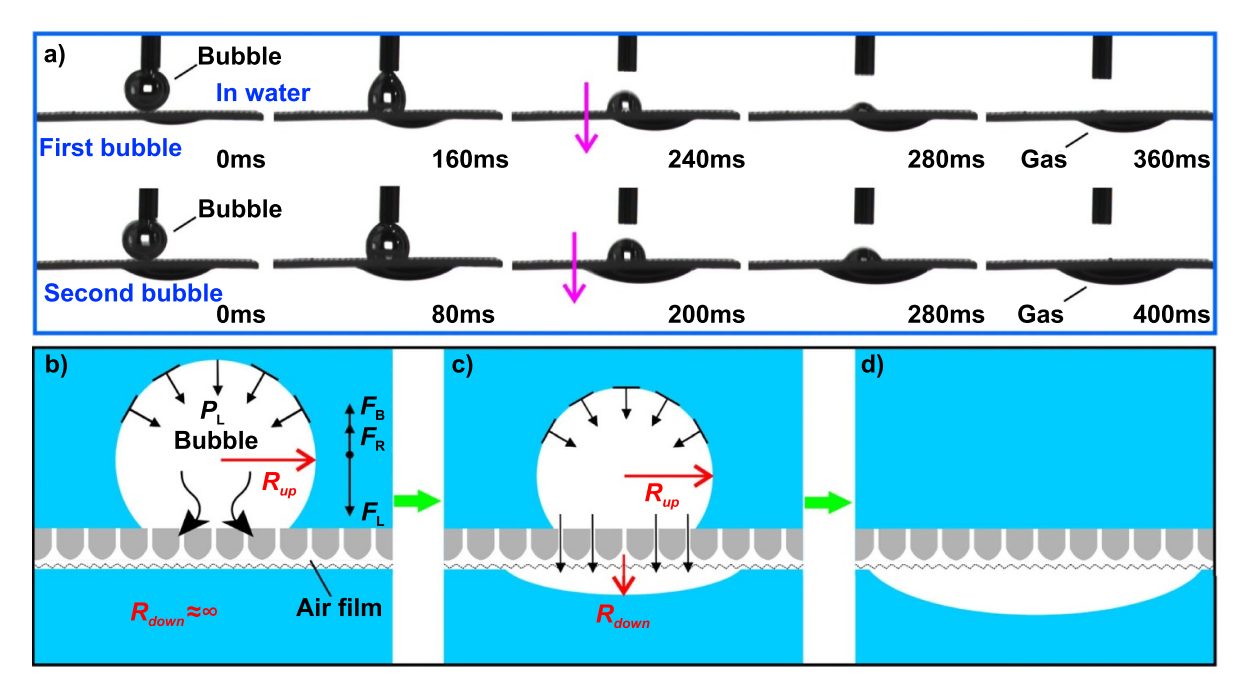


Figure 9. Anti-buoyancy unidirectional penetration of underwater gas bubbles through the as-prepared porous superwetting PTFE sheet. (a) Moving bubbles to contact the upper surface of the sheet. The big mouth of the microholes of the porous sheet is downward. (b-d) Underlying mechanism of bubbles penetrating the porous PTFE sheet from the upper side to the lower side (along the anti-buoyancy direction).

that greatly overcomes the $F_{\rm B}$ and $F_{\rm R}$. So, the Laplace pressure difference drives the gas to spontaneously transport downward (anti-buoyancy direction) (Figure 9(b-d)).

Similar to a diode, the function of the unidirectional gas passage ensures that the gas flows only along the particular direction in the water, preventing backflow. The superwetting porous sheet can be used to control the transporting direction in manipulating underwater gas. For the special case that one side of the porous sheet faces the water and another side faces air, bubbles in water can spontaneously pass through the sheet and be released into the atmosphere, enabling the porous sheet to separate gas bubbles from water.

2.4. Water/gas separation

Figure 10(a) depicts the schematic diagram of a device for eliminating tiny bubbles from a water pipeline. A branch part and a small hole are designed on the wall of the water pipeline. The laser-induced porous superhydrophobic and underwater superaerophilic PTFE sheet is used as the separation sheet and is mounted on the hole of the branch part. The excellent superhydrophobicity (water repellence) of the separation sheet ensures that water cannot leak out of the pipe. The bubbles in water flow move forward and can rise into the branch part because of the buoyancy. Once the bubbles contact the separation sheet, they will be absorbed by the superaerophilic microstructures and spontaneously pass through the pores. Finally, the gas in the bubbles is released into the external environment. As a result, the bubbles can pass through the separation sheet and are removed from the water flow. This strategy is verified by experiment. A manufactured simple separation device is prepared according to the proposed separation

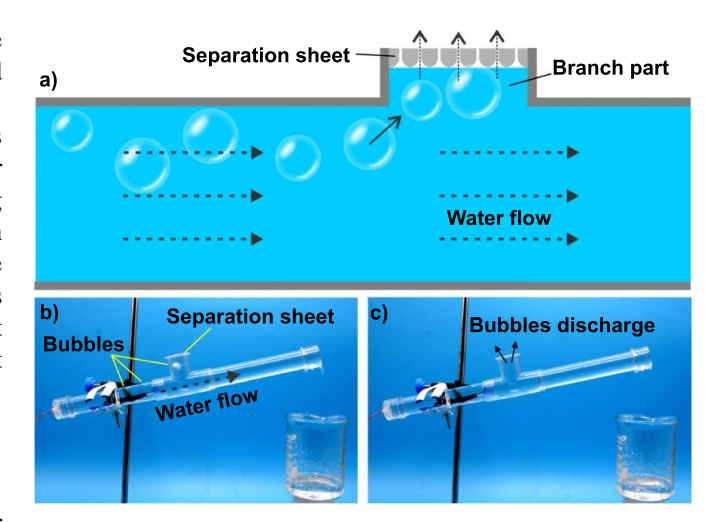


Figure 10. Removing bubbles in water flow by the laser-induced porous superhydrophobic and underwater superaerophilic PTFE sheet. (a) Schematic of the device for bubble removal from the water pipeline. (b), (c) Selected snapshots of bubbles being removed and released into the external environment: (b) bubbles moving forward with the water flow and rising into the branch part and (c) after a bubble penetrating the separation sheet.

mechanism, as shown in figure 10(b). Water normally flows in the pipeline. By contrast, all the bubbles in the water flow enter into the branch part and permeate through the separation sheet (figure 10(c) and movie S8 in the supporting information). The result indicates that the tiny bubbles in the water flow are removed from the water. Such a water/gas separation strategy can prevent the accumulation of bubbles in a channel related to the applications of microfluidics, liquid-based

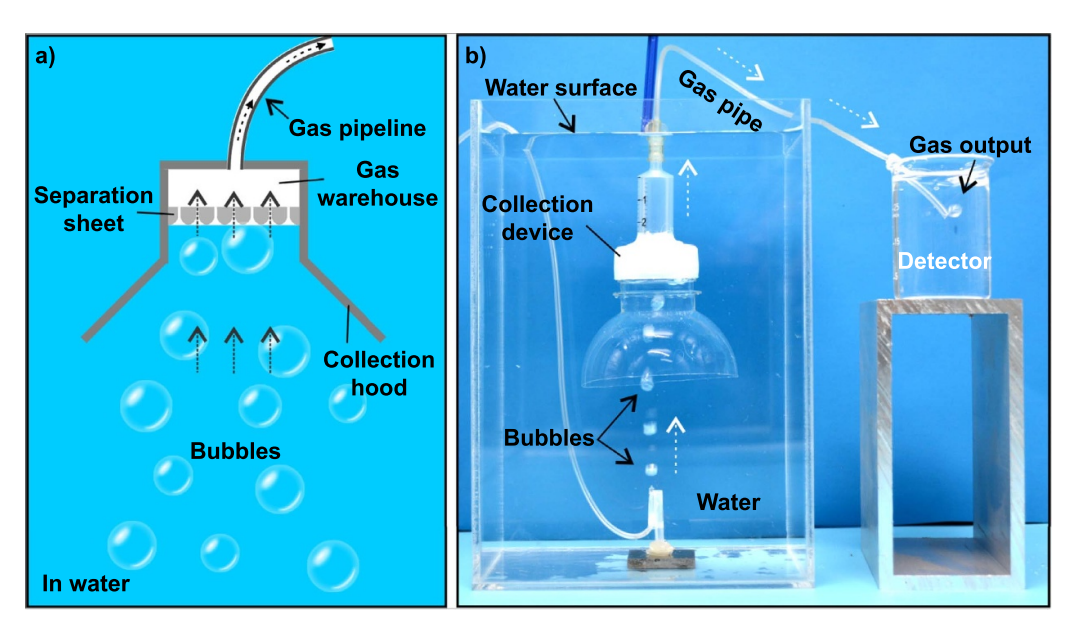


Figure 11. Collection of underwater gas bubbles by the laser-induced porous superhydrophobic and underwater superaerophilic PTFE sheet. (a) Schematic diagram of the device and mechanism of collecting bubbles from a liquid medium. (b) An artificial device which is collecting bubbles from water.

microanalysis systems, liquid-detecting instruments, infusion tubes, etc.

In addition to removing bubbles in a water pipeline, the as-prepared porous superwetting sheet can also be used to collect bubbles in a liquid. As shown in figure 11(a), a collection device composed of the hood, separation sheet, gas warehouse, and gas pipeline is proposed. The collection hood converges the rising bubbles onto the separation sheet. The surface microstructure of the laser-induced porous separation sheet is superhydrophobic in air and superaerophilic in water. The superhydrophobicity of the separation sheet prevents water from penetrating this sheet, and thereby water cannot flow into the collecting warehouse. In contrast, the bubbles can easily pass through the underwater superaerophilic separation sheet and thus enter into the gas warehouse. As a result, the bubbles in liquid are collected and provisionally stored in the gas warehouse. The collected gas can be timely transported to a user through a pipeline. Figure 11(b) and movie S9 (supporting information) show an artificial proof-of-concept device for underwater bubble collection. When the bubbles in water rise and contact the separation sheet, they can pass through the sheet and self-transport into the collecting chamber. To check whether the gas is collected and transported, we insert the end of the gas pipeline into the water. The output of gas bubbles reveals that the as-prepared device successfully collects the underwater gas bubbles, and the collected gas is transported along the gas pipeline. Such a device can be applied to collect valuable gas in a liquid, such as underwater energy gas.

Both the bubble removal and collection processes are based on gas self-transportation from the water side to the air side through the superwetting porous sheet. The removal or collection of underwater bubbles achieves the purpose of the separation of liquid and gas. Liquid/gas separation is an essential technology in chemical engineering, energy, and the environment.

3. Conclusions

We proposed a strategy to self-transport gas along the superhydrophobic and underwater superaerophilic open microchannels with a width even less than 100 μ m. Hierarchical micro/ nanostructures were easily produced on the inherently hydrophobic PTFE substrate by femtosecond laser processing, endowing the PTFE surface with excellent superhydrophobicity and underwater superaerophilicity. The water droplets on the resultant surface had a WCA of 154.0 \pm 0.7° and a WSA of $4.0 \pm 0.5^{\circ}$. In water, a small bubble completely spread over the PTFE surface with a final BCA of $\sim 0^{\circ}$. The femtosecond laser-induced superhydrophobic and underwater superaerophilic microgrooves supported gas transportation underwater because a hollow microchannel formed between the PTFE surface and water medium in water. Underwater gas was easily transported through this hollow microchannel. Interestingly, when superhydrophobic microgrooves connect different superhydrophobic regions in water, the gas spontaneously transfers from a small region to a large region. A unique laser drilling process can also integrate the microholes into the superhydrophobic and underwater superaerophilic PTFE sheet. The asymmetric morphology of the femtosecond laser-induced 'Y'-shaped microholes and the unique surface superwettability of the PTFE sheet allowed the gas bubbles to unidirectionally pass through the porous superwetting PTFE sheet (from the small-holes side to the big-holes side) in the water. Anti-buoyancy unidirectional penetration was achieved; that is, the gas overcame the buoyance of the bubble and self-transported downward. Similar to a diode, the function of the unidirectional gas passage of the superwetting porous sheet was used to determine the gas's transporting direction in manipulating underwater gas, preventing gas backflow. The Laplace pressure difference drove the processes of spontaneous gas transportation and unidirectional bubble passage. The superhydrophobic and underwater superaerophilic porous sheet were used to separate water and gas based on the behavior of gas self-transportation.

Femtosecond laser processing is a flexible technology that can directly write superhydrophobic and underwater superaerophilic microgrooves on the surface of a solid substrate and drill open microholes through a thin film. Furthermore, the track of the open microgrooves and the location of the open microholes can be accurately designed by the control program during laser processing. Although just the ordinary air bubble has been studied, it should be noticed that the driving force for gas transportation does not involve the chemical composition of the gas. Therefore, the manipulation of gas reported in this paper is applicable to other gases as long as they do not completely dissolve into the corresponding liquids.

We believe the reported methods of self-transporting gas in water along femtosecond laser-structured superhydrophobic and underwater superaerophilic microchannels will open up many new applications in energy utilization, chemical manufacturing, environmental protection, agricultural breeding, microfluidic chips, health care, etc.

4. Experimental section

4.1. Femtosecond laser processing

Figure 1(a) depicts the system of femtosecond laser processing. The PTFE sheet (thickness = 1 mm) is mounted on a computer-controlled translation platform. The 50 fs laser pulses (center wavelength = 800 nm; repetition rate = 1 kHz) are generated from a regenerative amplified Ti:sapphire system (Coherent Libra-usp-he) and are focused onto the PTFE surface through a plano-convex lens (focal length = 200 mm). The spot diameter of the focused laser beam is about 40 μ m. The PTFE substrate is processed by femtosecond laser based on the line-by-line laser scanning manner (figure 1(b)) [29, 41]. The laser fluence and the scanning speed are set constant at \sim 24 J cm⁻² (with a laser power of 300 μ J/pulse) and 5 mm s⁻¹ for ablating PTFE substrate, respectively. The interval (Λ) of the laser scanning lines is adjusted from 25 μm to 150 μ m by the control program. The laser-ablated PTFE surfaces are finally cleaned under ultrasound.

4.2. Preparation of the microgroove-connected circular regions

Three superhydrophobic circular regions with the diameter of 2 mm, 4 mm, and 6 mm are first prepared on the PTFE surface by the selective femtosecond laser processing, according to our previous work [31, 57]. Then, the femtosecond laser is used to write a single microgroove that connects these three

circular regions. The order of the three circles is adjusted, making the circles with different diameters possible to be in the middle.

4.3. Preparation of the 'Y'-shaped microholes array

The front side of a thin PTFE sheet (thickness = 0.3 mm) is previously treated by a femtosecond laser to prepare a superwetting surface microstructure. Then, 'Y'-shaped microholes are fabricated on the PTFE sheet. The preparation process of a microhole involves three steps: deceleration, stopover, and acceleration. For example, the distance between microholes is designed at 200 μ m. In the deceleration process, the relative translational speed of the laser-focused point to the PTFE sheet gradually decreases to 0 mm s⁻¹, with the laser point moving forward for 100 μ m. In the stopover process, the movement of the laser-focused point stops and stays here for 150 ms, allowing the femtosecond laser pulses to ablate through the PPFE sheet. Next, the laser point moves forward for another 100 μ m with its translational speed gradually increasing from 0 mm s⁻¹ (acceleration process). As a result, a single 'Y'-shaped microhole forms on the PTFE sheet. The movement direction of the laser point is perpendicular to the direction of the grooves of the pre-prepared superwetting microstructures. The accelerated speed is -5 mm s^{-2} in the deceleration process and 5 mm s⁻² in the acceleration process. By repeating the above fabrication process, a microhole array with a period of 200 μ m is obtained.

4.4. Characterization

The surface morphology of the PTFE sheet is observed by the FlexSEM-1000 (Hitachi, Japan) scanning electron microscopes. The contact angle and sliding angle of water droplets and underwater bubbles are measured by a JC2000D contactangle instrument (Powereach, China). The sliding angles are measured in the microgroove direction. The average values are obtained by measuring five different positions. The dynamic processes of droplet rolling and gas transporation are also recorded by the charge-coupled device (CCD) of the contactangle instrument. The processes of droplet rebounding, bubble spreading, and gas passage are captured by a high-speed CAMMC1362 camera (Mikrotron, Germany) at the frame rate of 2000 fps. The process of removing and collecting underwater bubbles is captured by a D7100 camera (Nikon, Japan).

Acknowledgments

This work is supported by the National Science Foundation of China under the Grant Nos. 61875158 and 61805192, the National Key Research and Development Program of China under the Grant No. 2017YFB1104700, the International Joint Research Laboratory for Micro/Nano Manufacturing and Measurement Technologies, and the Fundamental Research Funds for the Central Universities.

Conflict of interest

There are no conflicts to declare.

ORCID iD

Feng Chen https://orcid.org/0000-0002-7031-7404

References

- [1] Liu X C, Yang F C, Guo J, Fu J and Guo Z G 2020 New insights into unusual droplets: from mediating the wettability to manipulating the locomotion modes *Chem. Commun.* 56 14757–88
- [2] Tang X, Tian Y, Tian X W, Li W, Han X, Kong T T and Wang L Q 2021 Design of multi-scale textured surfaces for unconventional liquid harnessing *Mater. Today* 43 62–83
- [3] Su B, Tian Y and Jiang L 2016 Bioinspired interfaces with superwettability: from materials to chemistry *J. Am. Chem. Soc.* **138** 1727–48
- [4] Yong J L, Zhuang J, Bai X, Huo J L, Yang Q, Hou X and Chen F 2021 Water/gas separation based on the selective bubble-passage effect of underwater superaerophobic and superaerophilic meshes processed by a femtosecond laser *Nanoscale* 13 10414–24
- [5] Lu Z Y et al 2014 Ultrahigh hydrogen evolution performance of under-water "superaerophobic" MoS₂ nanostructured electrodes Adv. Mater. 26 2683–7
- [6] Lu Z Y, Li Y J, Lei X D, Liu J F and Sun X M 2015 Nanoarray based "superaerophobic" surfaces for gas evolution reaction electrodes *Mater. Horiz.* 2 294–8
- [7] Lu Z Y, Sun M, Xu T H, Li Y J, Xu W W, Chang Z, Ding Y, Sun X M and Jiang L 2015 Superaerophobic electrodes for direct hydrazine fuel cells Adv. Mater. 27 2361–6
- [8] Chen X, Wu Y C, Su B, Wang J M, Song Y L and Jiang L 2012 Terminating marine methane bubbles by superhydrophobic sponges Adv. Mater. 24 5884–9
- [9] Yu C M, Cao M Y, Dong Z C, Li K, Yu C L, Wang J M and Jiang L 2016 Aerophilic electrode with cone shape for continuous generation and efficient collection of H₂ bubbles Adv. Funct. Mater. 26 6830-5
- [10] Zhu S W, Li J W, Cai S, Bian Y C, Chen C, Xu B, Su Y H, Hu Y L, Wu D and Chu J R 2020 Unidirectional transport and effective collection of underwater CO₂ bubbles utilizing ultrafast-laser-ablated Janus foam ACS Appl. Mater. Interfaces 12 18110–5
- [11] Ma H Y, Cao M Y, Zhang C H, Bei Z L, Li K, Yu C M and Jiang L 2018 Directional and continuous transport of gas bubbles on superaerophilic geometry-gradient surfaces in aqueous environments Adv. Funct. Mater. 28 1705091
- [12] Yu C M, Cao M Y, Dong Z C, Wang J M, Li K and Jiang L 2016 Spontaneous and directional transportation of gas bubbles on superhydrophobic cones Adv. Funct. Mater. 26 3236–43
- [13] Vorobyev A Y and Guo C L 2013 Direct femtosecond laser surface nano/microstructuring and its applications *Laser Photonics Rev.* 7 385–407
- [14] Stratakis E *et al* 2020 Laser engineering of biomimetic surfaces *Mater. Sci. Eng. R.* **141** 100562
- [15] Sugioka K and Cheng Y 2014 Ultrafast lasers-reliable tools for advanced materials processing *Light Sci. Appl.* 3 e149
- [16] Liu X Q, Bai B F, Chen Q D and Sun H B 2019 Etching-assisted femtosecond laser modification of hard materials *Opto Electron. Adv.* 2 190021
- [17] Chong T C, Hong M H and Shi L P 2010 Laser precision engineering: from microfabrication to nanoprocessing *Laser Photonics Rev.* 4 123–43

- [18] Sugioka K and Cheng Y 2014 Femtosecond laser three-dimensional micro- and nanofabrication Appl. Phys. Rev. 1 041303
- [19] Yong J L, Yang Q, Guo C L, Chen F and Hou X 2019 A review of femtosecond laser-structured superhydrophobic or underwater superoleophobic porous surfaces/materials for efficient oil/water separation RSC Adv. 9 12470–95
- [20] Chen F, Zhang D S, Yang Q, Yong J L, Du G Q, Si J H, Yun F and Hou X 2013 Bioinspired wetting surface via laser microfabrication ACS Appl. Mater. Interfaces 5 6777–92
- [21] Yong J L, Chen F, Yang Q and Hou X 2015 Femtosecond laser controlled wettability of solid surfaces Soft Matter 11 8897–906
- [22] Yong J L, Chen F, Yang Q, Jiang Z D and Hou X 2018 A review of femtosecond-laser-induced underwater superoleophobic surfaces Adv. Mater. Interfaces 5 1701370
- [23] Stratakis E, Ranella A and Fotakis C 2011 Biomimetic micro/nanostructured functional surfaces for microfluidic and tissue engineering applications *Biomicrofluidics* 5 013411
- [24] Pazokian H, Selimis A, Barzin J, Jelvani S, Mollabashi M, Fotakis C and Stratakis E 2012 Tailoring the wetting properties of polymers from highly hydrophilic to superhydrophobic using UV laser pulses *J. Micromech. Microeng.* 22 035001
- [25] Baldacchini T, Carey J E, Zhou M and Mazur E 2006 Superhydrophobic surfaces prepared by microstructuring of silicon using a femtosecond laser *Langmuir* 22 4917–9
- [26] Zorba V, Stratakis E, Barberoglou M, Spanakis E, Tzanetakis P, Anastasiadis S H and Fotakis C 2008 Biomimetic artificial surfaces quantitatively reproduce the water repellency of a lotus leaf Adv. Mater. 20 4049–54
- [27] Yong J L, Chen F, Yang Q, Zhang D S, Bian H, Du G Q, Si J H, Meng X W and Xou X 2013 Controllable adhesive superhydrophobic surfaces based on PDMS microwell arrays *Langmuir* 29 3274–9
- [28] Yong J L, Chen F, Yang Q, Zhang D S, Du G Q, Si J H, Yun F and Hou X 2013 Femtosecond laser weaving superhydrophobic patterned PDMS surfaces with tunable adhesion J. Phys. Chem. C 117 24907–12
- [29] Yong J L, Yang Q, Chen F, Zhang D S, Farooq U, Du G Q and Hou X 2014 A simple way to achieve superhydrophobicity, controllable water adhesion, anisotropic sliding, and anisotropic wetting based on femtosecond-laser-induced line-patterned surfaces J. Mater. Chem. A 2 5499–507
- [30] Yong J L, Yang Q, Chen F, Zhang D S, Du G Q, Bian H, Si J H, Yun F and Hou X 2014 Superhydrophobic PDMS surfaces with three-dimensional (3D) pattern-dependent controllable adhesion Appl. Surf. Sci. 288 579–83
- [31] Yong J L, Fang Y, Chen F, Huo J L, Yang Q, Bian H, Du G Q and Hou X 2016 Femtosecond laser ablated durable superhydrophobic PTFE films with micro-through-holes for oil/water separation: separating oil from water and corrosive solutions *Appl. Surf. Sci.* 389 1148–55
- [32] Yu C M, Zhang P P, Wang J M and Jiang L 2017 Superwettability of gas bubbles and its application: from bioinspiration to advanced materials Adv. Mater. 29 1703053
- [33] George J E, Chidangil S and George S D 2017 Recent progress in fabricating superaerophobic and superaerophilic surfaces Adv. Mater. Interfaces 4 1601088
- [34] Tian Y, Su B and Jiang L 2014 Interfacial material system exhibiting superwettability *Adv. Mater.* **26** 6872–97
- [35] Yong J L, Singh S C, Zhan Z B, Chen F and Guo C L 2019 How to obtain six different superwettabilities on a same microstructured pattern: relationship between various superwettabilities in different solid/liquid/gas systems Langmuir 35 921–7

- [36] Zhang D S and Sugioka K 2019 Hierarchical microstructures with high spatial frequency laser induced periodic surface structures possessing different orientations created by femtosecond laser ablation of silicon in liquids *Opto Electron. Adv.* 2 190002
- [37] Zhang Y Y, Jiao Y L, Li C Z, Chen C, Li J W, Hu Y L, Wu D and Chu J R 2020 Bioinspired micro/nanostructured surfaces prepared by femtosecond laser direct writing for multi-functional applications *Int. J. Extreme Manuf.* 2,032002
- [38] Bai X, Yang Q, Fang Y, Zhang J Z, Yong J L, Hou X and Chen F 2020 Superhydrophobicity-memory surfaces prepared by a femtosecond laser *Chem. Eng. J.* 383 123143
- [39] Shen M Y, Crouch C H, Carey J E and Mazur E 2004 Femtosecond laser-induced formation of submicrometer spikes on silicon in water Appl. Phys. Lett. 85 5694–6
- [40] Shan C, Chen F, Yang Q, Li Y Y, Bian H, Yong J L and Hou X 2015 High-level integration of three-dimensional microcoils array in fused silica Opt. Lett. 40 4050–3
- [41] Yong J L, Singh S C, Zhan Z B, EIKabbash M, Chen F and Guo C L 2019 Femtosecond-laser-produced underwater "superpolymphobic" nanorippled surfaces: repelling liquid polymers in water for applications of controlling polymer shape and adhesion ACS Appl. Nano Mater. 2 7362–71
- [42] Larmour I A, Bell S E J and Saunders G C 2007 Remarkably simple fabrication of superhydrophobic surfaces using electroless galvanic deposition *Angew. Chem.* 119 1740–2
- [43] Yong J L, Chen F, Li M J, Yang Q, Fang Y, Huo J L and Hou X 2017 Remarkably simple achievement of superhydrophobicity, superhydrophilicity, underwater superoleophobicity, underwater superoleophilicity, underwater superaerophobicity, and underwater superaerophilicity on femtosecond laser ablated PDMS surfaces J. Mater. Chem. A 5 25249–57
- [44] Yong J L, Chen F, Yang Q, Huo J L and Hou X 2017 Superoleophobic surfaces Chem. Soc. Rev. 46 4168–217
- [45] Cassie A B D and Baxter S 1944 Wettability of porous surfaces Trans. Faraday Soc. 40 546–51
- [46] Wang S and Jiang L 2007 Definition of superhydrophobic states Adv. Mater. 19 3423–4

- [47] Pei C T, Peng Y, Zhang Y, Tian D L, Liu K S and Jiang L 2018 An integrated Janus mesh: underwater bubble antibuoyancy unidirectional penetration ACS Nano 12 5489–94
- [48] Yan S G *et al* 2018 Unidirectional self-transport of air bubble via a Janus membrane in aqueous environment *Appl. Phys. Lett.* **113** 261602
- [49] Zhang C H, Zhang B, Ma H Y, Li Z, Xiao X, Zhang Y H, Cui X Y, Yu C M, Cao M Y and Jiang L 2018 Bioinspired pressure-tolerant asymmetric slippery surface for continuous self-transport of gas bubbles in aqueous environment ACS Nano 12 2048–55
- [50] Liu G L, Zhang C H, Liu M F, Guo Z W, Wang X S, Yu C M and Cao M Y 2020 Smart manipulation of gas bubbles in harsh environments via a fluorinert-infused shape-gradient slippery surface *Trans. Tianjin Univ.* 26 441–9
- [51] Yong J L, Chen F, Fang Y, Huo J L, Yang Q, Zhang J Z, Bian H and Hou X 2017 Bioinspired design of underwater superaerophobic and superaerophilic surfaces by femtosecond laser ablation for anti- or capturing bubbles ACS Appl. Mater. Interfaces 9 39863–71
- [52] Huo J L, Yong J L, Chen F, Yang Q, Fang Y and Hou X 2019 Trapped air-induced reversible transition between underwater superaerophilicity and superaerophobicity on the femtosecond laser-ablated superhydrophobic PTFE surfaces Adv. Mater. Interfaces 6 1900262
- [53] Sackmann E K, Fulton A L and Beebe D J 2014 The present and future role of microfluidics in biomedical research *Nature* 507 181–9
- [54] Shang L R, Cheng Y and Zhao Y J 2017 Emerging droplet microfluidics Chem. Rev. 117 7964–8040
- [55] Zhang J, Yan S, Yuan D, Alici G, Nguyen N T, Warkiani M E and Li W H 2016 Fundamentals and applications of inertial microfluidics: a review *Lab Chip* 16 10–34
- [56] Long J Y, Fan P X, Jiang D E, Han J P, Lin Y, Cai M Y, Zhang H J and Zhong M L 2016 Anisotropic sliding of water droplets on the superhydrophobic surfaces with anisotropic groove-like micro/nano structures Adv. Mater. Interfaces 3 1600641
- [57] Yong J L, Chen F, Yang Q, Farooq U and Hou X 2015 Photoinduced switchable underwater superoleophobicity-superoleophilicity on laser modified titanium surfaces J. Mater. Chem. A 3 10703–9